MXenes for Plasmonic Photodetection

Dhinesh Babu Velusamy, Jehad K. El-Demellawi, Ahmed M. El-Zohry, Andrea Giugni, Sergei Lopatin, Mohamed N. Hedhili, Ahmed E. Mansour, Enzo Di Fabrizio, Omar F. Mohammed, and Husam N. Alshareef*

MXenes have recently shown impressive optical and plasmonic properties associated with their ultrathin-atomic-layer structure. However, their potential use in photonic and plasmonic devices has been only marginally explored. Photodetectors made of five different MXenes are fabricated, among which molybdenum carbide MXene (Mo_2CT_x) exhibits the best performance. Mo_2CT_x MXene thin films deposited on paper substrates exhibit broad photoresponse in the range of 400–800 nm with high responsivity (up to 9 A W^{-1}), detectivity ($\approx 5 \times 10^{11}$ Jones), and reliable photoswitching characteristics at a wavelength of 660 nm. Spatially resolved electron energy-loss spectroscopy and ultrafast femtosecond transient absorption spectroscopy of the MXene nanosheets reveal that the photoresponse of Mo_2CT_x is strongly dependent on its surface plasmon-assisted hot carriers. Additionally, Mo_2CT_x thin-film devices are shown to be relatively stable under ambient conditions, continuous illumination and mechanical stresses, illustrating their durable photodetection operation in the visible spectral range. Micro-Raman spectroscopy conducted on bare Mo_2CT_x film and on gold electrodes allowing for surface-enhanced Raman scattering demonstrates surface chemistry and a specific low-frequency band that is related to the vibrational modes of the single nanosheets. The specific ability to detect and excite individual surface plasmon modes provides a viable platform for various MXene-based optoelectronic applications.

MXenes, a thriving family of transition metal-based 2D materials, have garnered significant interest due to their intriguing physicochemical properties and solution processability.[1–11] 2D MXene nanosheets are obtained by selectively etching away the A atoms from their parent ternary "MAX" phases constituting a large family of layered transition metal carbides, nitrides, or carbonitrides. The synthesized 2D MXenes have the general formula: $M_{n+1}X_nT_x$, where "M" is an early transition metal,

"A" is an A-group element, e.g., Al, Ga, Si, etc., "X" is carbon and/or nitrogen, and T denotes the surface-terminated functional groups such as −OH, −F, and −O,[1] and x in T_x represents the population of those surface-terminated moieties. Thus far, owing to their promising electrochemical characteristics, this new class of 2D materials has been predominantly used in energy conversion and storage applications.[2,3,12,13] Nonetheless, they have also endowed fascinating prospects for a variety of emerging applications in electronics, sensing, and photonics.[2,14–16] In this regard, MXenes have recently exhibited impressive optical properties, e.g., tunable broadband absorption[16–18] and intense surface plasmon excitations,[19,20] underlining their potential for optoelectronic and plasmonic applications. However, theoretical[20] and experimental investigations[16,21,22] in this context remain sparse and mainly limited to the most studied $Ti_3C_2T_x$ MXene.

In this work, five different MXene nanosheets, i.e., Mo_2CT_x, $Ti_3C_2T_x$, Nb_2CT_x, T_2CT_x, and V_2CT_x, were first synthesized from their parent MAX phases (see the Experimental Section in the Supporting Information for the detailed synthesis of MAX and MXenes). Their structural, morphological, and steady-state optical characteristics are displayed in Figures S1–S6 in the Supporting Information. Among the five studied MXenes, Mo_2CT_x was selected as a model system for its relative stability against oxidation, moderately high free carrier density, and electrical conductivity,[7] though not as high as $Ti_3C_2T_x$.[2,18,19] In principle, for the sake of not having high dark currents, materials with metal-like conductivity are not preferred for photodetectors.

In this regard, for the first time, we demonstrate Mo_2CT_x thin film photodetectors that operate in the visible spectral region. The optoelectronic properties of the mechanically flexible arrays of two-terminal, parallel-type photodetectors based on Mo_2CT_x MXene thin films deposited on paper substrates (nylon membrane filters) are thoroughly investigated. We show that the responsivity and detectivity of the Mo_2CT_x photodetectors can reach as high as 9 A W^{-1} and $\approx 5 \times 10^{11}$ Jones, respectively, at a wavelength of 660 nm. It is worth mentioning that the responsivity of the Mo_2CT_x MXene devices we propose is $\approx 18\,000$ and ≈ 1200 times higher than the first reported graphene[23]

Dr. D. B. Velusamy, J. K. El-Demellawi, Dr. A. M. El-Zohry, Dr. A. Giugni, Dr. A. E. Mansour, Prof. E. Di Fabrizio, Prof. O. F. Mohammed, Prof. H. N. Alshareef
Physical Science and Engineering Division
King Abdullah University of Science and Technology (KAUST)
Thuwal 23955-6900, Kingdom of Saudi Arabia
E-mail: husam.alshareef@kaust.edu.sa
Dr. S. Lopatin, Dr. M. N. Hedhili
Core Labs
King Abdullah University of Science and Technology (KAUST)
Thuwal 23955-6900, Kingdom of Saudi Arabia

**ADVANCED
SCIENCE NEWS**

www.advancedsciencenews.com

**ADVANCED
MATERIALS**

www.advmat.de

and MoS_2[24] photodetectors, respectively. We found that the photocurrent in Mo_2CT_x is principally controlled by efficient surface plasmon-assisted hot electron generation. The MXene films, composed of the disordered superposition of crystalline nanosheets with dimensions about hundreds of nanometers, offer naturally high density of edges and nanometric gaps that can efficiently relax plasmonic momentum constraints promoting energized hot electrons generation.[25] The relatively lower electronic density of Mo_2CT_x (i.e., $\approx 3 \times 10^{20}$ cm^{-3}),[7] with respect to conventional plasmonic metals, allows for a longer electronic mean free path, supporting a rather long experimental electron–electron scattering relaxation time and the very good performances reported here. The existence and the distribution of a variety of surface plasmon modes over individual Mo_2CT_x nanosheets are visualized by the combination of scanning transmission electron microscopy (STEM) and ultrahigh resolution electron energy loss spectroscopy (EELS). The dynamics of the generated plasmon-assisted hot carriers upon excitation is elucidated using femtosecond visible transient absorption experiments. We also show that Mo_2CT_x-based devices have maintained over 80% of the initial photocurrent generation efficiency even after 12 000 s of continuous illumination of 660 nm light. While the I_{on}/I_{off} ratio remained almost the same over the course of 30+ days of storage under vacuum at room temperature. Moreover, the arrays of Mo_2CT_x thin film photodetectors are shown to be readily bendable under multiple and repeated deformations.

Figure 1a shows a schematic representation of a Mo_2CT_x nanosheet, where one layer of carbon is sandwiched between two layers of molybdenum, while the surface of the nanosheet is randomly terminated with functional surface moieties, i.e., −OH, −O, and −F. The transmission electron microscopy (TEM) image and corresponding selected area electron diffraction (SAED) pattern of Mo_2CT_x nanosheets show a smooth surface morphology with a high crystal quality (Figure 1b). Further, the atomic-resolution scanning transmission electron microscopy image of Mo_2CT_x nanosheets (Figure 1c) indicates the hexagonal structure of the basal planes without obvious nanometer-scale defects or carbide amorphization.[8] The UV–vis–NIR absorption spectra of as-prepared suspension of Mo_2CT_x nanosheets in water (0.6 mg mL^{-1}, red) and a ≈ 1.8 µm thick film of Mo_2CT_x (blue) are depicted in Figure 1d. The difference between the absorption of film and suspension is attributed to light scattering by the suspended colloidal Mo_2CT_x nanosheets, which is almost negligible for the Mo_2CT_x film. The inset of Figure 1d is indicative of the Tyndall scattering effect confirming the colloidal nature and the stability of Mo_2CT_x suspensions in water. The V-shape spectra indicate the presence of free carrier absorption, which typically occurs at longer wavelengths for other materials with low free carrier density.[26] However, owing to the higher free carrier concentration of Mo_2CT_x,[7] the whole absorption spectra are featured at shorter wavelengths with a minimum (absorption coefficient, α, of 57 cm^{-1}) at ≈ 250 nm, representing the onset of free carrier absorption. In Figure 1d, the left gray-shaded part denotes the absorption range dominated by the interband transition (IBT) between valence and conduction bands. While at wavelengths between ≈ 230 and 330 nm, the intraconduction band absorption is stronger than the relatively weak free carrier absorption,[26]

which becomes dominant above ≈ 350 nm. The widespread absorption of Mo_2CT_x nanosheets makes it appealing for photodetectors operating in the visible spectral region.

For further investigations, homogeneous MXene thin films (≈ 2 µm thick) were deposited on nylon membranes (filter papers) via vacuum-assisted filtration from MXene suspensions. The corresponding X-ray diffraction (XRD) patterns of films made of intercalated- and exfoliated-Mo_2CT_x are shown in Figure 1e in comparison to XRD of their parent MAX phase (Mo_2Ga_2C powder). The shift in the (002) peak toward lower angles indicates an increase in the d-spacing and c-lattice parameter compared to their parent MAX phase.[27] The (002) peak for exfoliated-Mo_2CT_x, which is partially intercalated with water,[3,28] is observed at 8.9°, but it was shifted to 4.5° for intercalated-Mo_2CT_x upon further intercalation using tetrabutylammonium hydroxide as explained in the Supporting Information.[27] The scanning electron microscopy (SEM) image (Figure 1f) shows that the fabricated Mo_2CT_x thin film (Figure 1g) is composed of few-layer Mo_2CT_x nanosheets stacked together with their surfaces preferentially aligned parallel to the film.

Furthermore, X-ray photoelectron spectroscopy (XPS) was performed on the fabricated MXene thin films to study their chemical compositions and oxidation states. The corresponding high-resolution XPS spectra for Mo 3d and C 1s in Mo_2CT_x are depicted in Figure 1i,j. The Mo 3d core level (Mo 3d$_{5/2}$ − Mo 3d$_{3/2}$) of the Mo_2CT_x sample was fitted with four doublets (eight components) with a fixed area ratio equal to 3:2 and doublet separation of 3.18 eV. The Mo 3d$_{5/2}$ components were located at 228.2, 229.3, 230.9, and 232.1 eV, respectively. The Mo 3d$_{5/2}$ component centered at 228.2 eV is associated with unterminated Mo bound to C present in Mo_2CT_x and with traces of Mo_2Ga_2C.[27,29] While the Mo 3d$_{5/2}$ component centered at 229.3 eV is assigned to surface Mo atoms bound to C in Mo_2CT_x nanosheets, where Mo is bound to surface termination species such as O, OH, and/or F.[27,30] Additionally, the Mo 3d$_{5/2}$ components centered at 230.9 and 232.1 eV are attributed to Mo^{5+} and Mo^{6+} oxidized species, respectively, arising from the inevitable surface oxidation during air exposure.[27,31] The detected Mo^{6+} specie mainly exists in the form of the amorphous MoO_3 and possibly in the form of Mo_4O_{11}, which is comprised of Mo^{5+} besides the Mo^{6+} specie.[32,33] Mo^{5+} may also exist in the form of Mo_2O_5,[34,35] which is known to be unstable in air, and readily oxidizes to MoO_3.[34] Likewise, other possible phases of Mo^{5+} hydroxyoxides (e.g., $MoO(OH)_3$ and $MoO_2(OH)$) are also known to spontaneously oxidize in air forming Mo^{6+} phases.[36] Accordingly, by the time our devices are measured in air, any possible amount of Mo^{5+} hydroxyoxides or oxides, other than Mo_4O_{11}, would wane in favor of forming more Mo^{6+} oxides. Anyway, it is noteworthy that Mo^{5+}-based phases are expected to be very minimal owing to the low content of the Mo^{5+} specie ($\approx 7\%$) within the sampling depth of XPS (Figure 1i). Meanwhile, the Mo bound to C in Mo_2CT_x remains to be the most abundant species with more than 50% of the total Mo atoms present in the XPS sampling depth of the MXene film.

The high-resolution spectrum for C 1s core level of Mo_2CT_x (Figure 1j) was also fitted using seven components located at 283.1, 283.8, 284.4, 284.8, 286.2, 288.1, and 290.4 eV corresponding to C−Mo, C−Mo−O, C=C (sp2), C−C/C−H (sp3), C−O, C=O, and (O−C=O and C−F) bonds, respectively.[27]
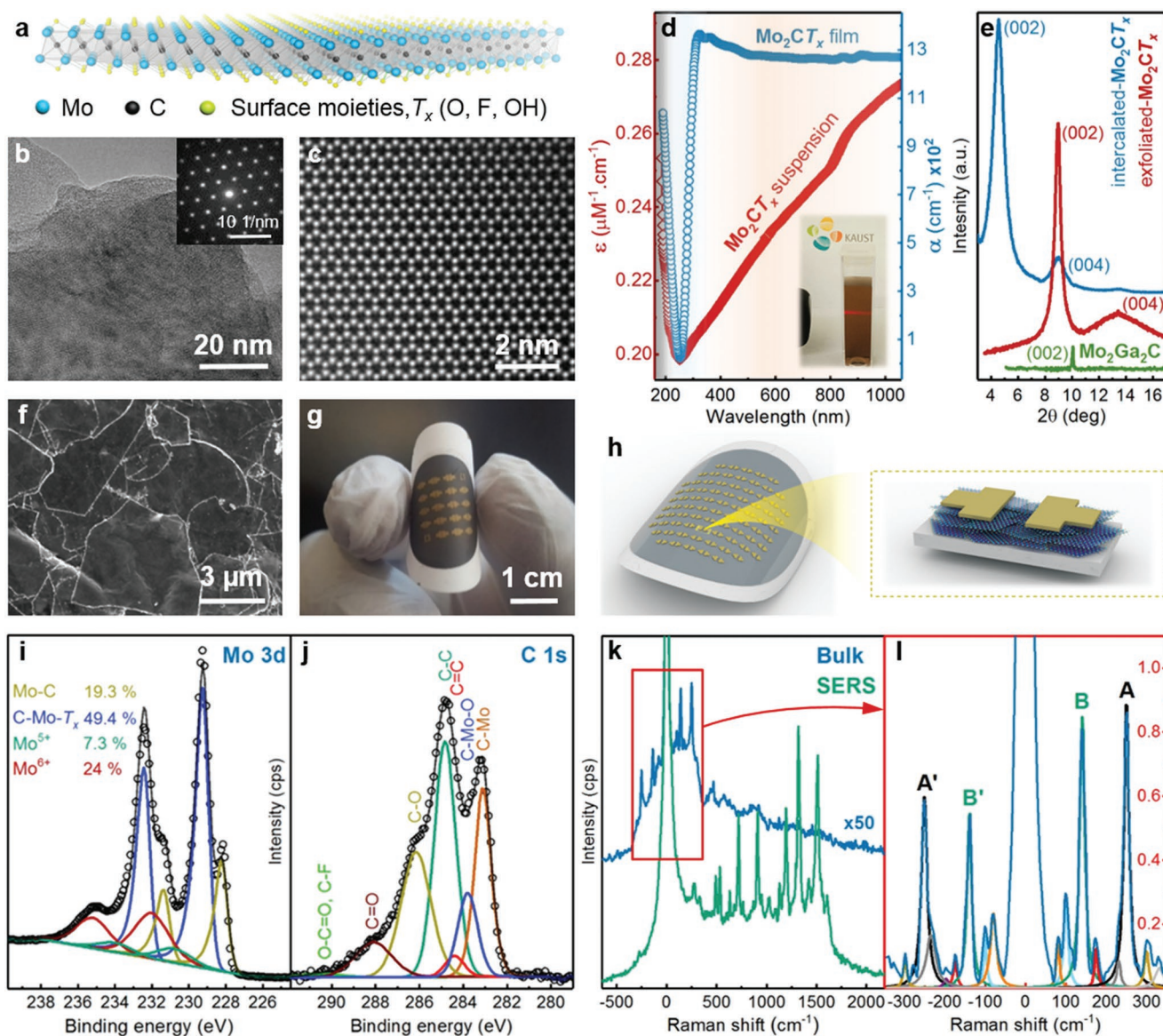
Figure 1. a) Schematic illustration of a delaminated Mo_2CT_x nanosheet: One layer of carbon is sandwiched between two layers of Molybdenum and the surface is randomly terminated with functional surface moieties, T_x: (—OH, —O, and —F)$_x$. b) TEM image of few-layered Mo_2CT_x nanosheets. Inset: Fast Fourier transform (FFT) pattern. c) High-resolution STEM image of Mo_2CT_x. Note the hexagonal structure of the basal planes and high crystallinity of the Mo_2CT_x nanosheet with no obvious nanometer-scale defects. d) UV–vis–NIR absorption spectra of Mo_2CT_x film (blue, 1.8 µm) and dispersed in water (red, 0.6 mg mL^{-1}) with a minimum at ≈250 nm, representing the onset of free carrier absorption. Inset: A photograph showing the Tyndall scattering effect in stable colloidal water-suspension of Mo_2CT_x nanosheets. e) XRD patterns (vertically displaced for clarity) of Mo_2Ga_2C (green), exfoliated-Mo_2CT_x (red), and intercalated-Mo_2CT_x (blue) at low Bragg's angles. f) SEM micrograph showing the surface morphology of a Mo_2CT_x thin film. g) Photograph and h) schematic illustration of an array of two-terminal, parallel-type thin film Mo_2CT_x-based flexible photodetectors. i) High-resolution XPS spectrum of the Mo 3d and j) C 1s core levels. k) Micro-Raman spectroscopy of Mo_2CT_x at 633 nm. (Blue) Resonant Raman scattering spectrum of Mo_2CT_x (Bulk, obtained by averaging more than 1000 spectra). (Green) A surface-enhanced Raman scattering (SERS) spectrum, displayed for comparison, obtained at one position on the Au electrodes. l) Low-frequency range of the Raman spectrum of the bare Mo_2CT_x film. The spectrum is analyzed by Lorentzian functions after subtraction of the broad baseline.

Figure S7 in the Supporting Information displays the high-resolution XPS spectra of F 1s and O 1s regions of the Mo_2CT_x film. The corresponding high-resolution XPS spectra of the other studied MXenes ($Ti_3C_2T_x$, Nb_2CT_x, T_2CT_x, and V_2CT_x) are displayed in Figures S8–S11 in the Supporting Information.

Next, e-beam evaporation was used to deposit gold electrodes (≈50 nm thick) on the fabricated Mo_2CT_x films, giving rise to mechanically flexible arrays of two-terminal, parallel-type devices with a channel length and width of 70 µm and 1 mm, respectively (see Figure 1g,h). Thereupon, these Mo_2CT_x films were characterized by micro-Raman spectroscopy imaging in large areas across the two electrodes of single devices. The corresponding spectral analysis (Figure 1k,l) unveiled the low-frequency fingerprint spectrum of our Mo_2CT_x MXene and

**ADVANCED
SCIENCE NEWS**

www.advancedsciencenews.com

**ADVANCED
MATERIALS**

www.advmat.de

elucidated a significant heterogeneity of its surface chemistry. By exploiting the surface-enhanced Raman scattering (SERS) effect, triggered by the Au electrodes, we were able to measure signals arising from nanoscale volumes defined by nanogaps and confined on the outer most surface of the nanosheets. The measured signals have evidenced a very high spectral variability, at submicron scale level, in the high-frequency range, i.e., above 600 cm^{-1}. In contrast, bare Mo$_2$CT$_x$ scattering results, though of very small intensity, were spatially quite uniform. Thus, by averaging hundreds of consecutive spectra, it was possible to identify the main molecular vibrational modes within the Mo$_2$CT$_x$ network including shear and interlayer breathing modes. The Lorentzian shape analysis of the Stokes (S) and anti-Stokes (AS) sides of the spectrum (Figure 1l) in the (−500, 500) cm^{-1} range allowed for the identification of up to ten vibrations with high accuracy. The assignment of the identified peaks is summarized in Table S1 in the Supporting Information, and detailed in the Supporting Information. We have also highlighted a photon–electron–phonon anisotropic resonance process relying on the observed anomalously low S/AS intensity ratios: ≈1.3. Interestingly, such a value is rather far from what can be estimated (≈10) for considered peak couples, $\Delta\nu_{S\text{-}AS} = 500$ cm^{-1}, following the Bose–Einstein statistics, generally used to describe

thermally activated phononic excitations. For more details, refer to Figures S12–S14 in the Supporting Information and the corresponding Raman structural characterization.

Next, to study the broadband visible photoresponse of MXene thin films, we measured their spectral sensitivity as a function of wavelength. In particular, we have examined Mo$_2$CT$_x$ thin films in the 400–800 nm range focusing the tunable radiation of a supercontinuum white laser excitation on a spot size of ≤25 μm at the center between the electrodes (70 μm apart), partially on one electrode and on a large area covering the whole device by simply defocusing the illumination (**Figure 2**a; Figure S15, Supporting Information). The spectral profile of thin films made of Mo$_2$CT$_x$ demonstrated a spectral response in the range of 500 to 800 nm (Figure 2a; Figure S15b, Supporting Information), highlighting the resonant response of the device in the visible region. This spectral response lies within the window of free carrier absorption as illustrated in the measured UV–vis–NIR absorption spectrum of Mo$_2$CT$_x$ (Figure 1d). Furthermore, we performed a fixed bias (0.5V) micro-photocurrent imaging as shown in Figure S16 in the Supporting Information. The corresponding micro-photocurrent map, obtained at a representative wavelength of 633 nm, is in agreement with the spectral sensitivity of Mo$_2$CT$_x$ devices. It shows a rather homogeneous signal
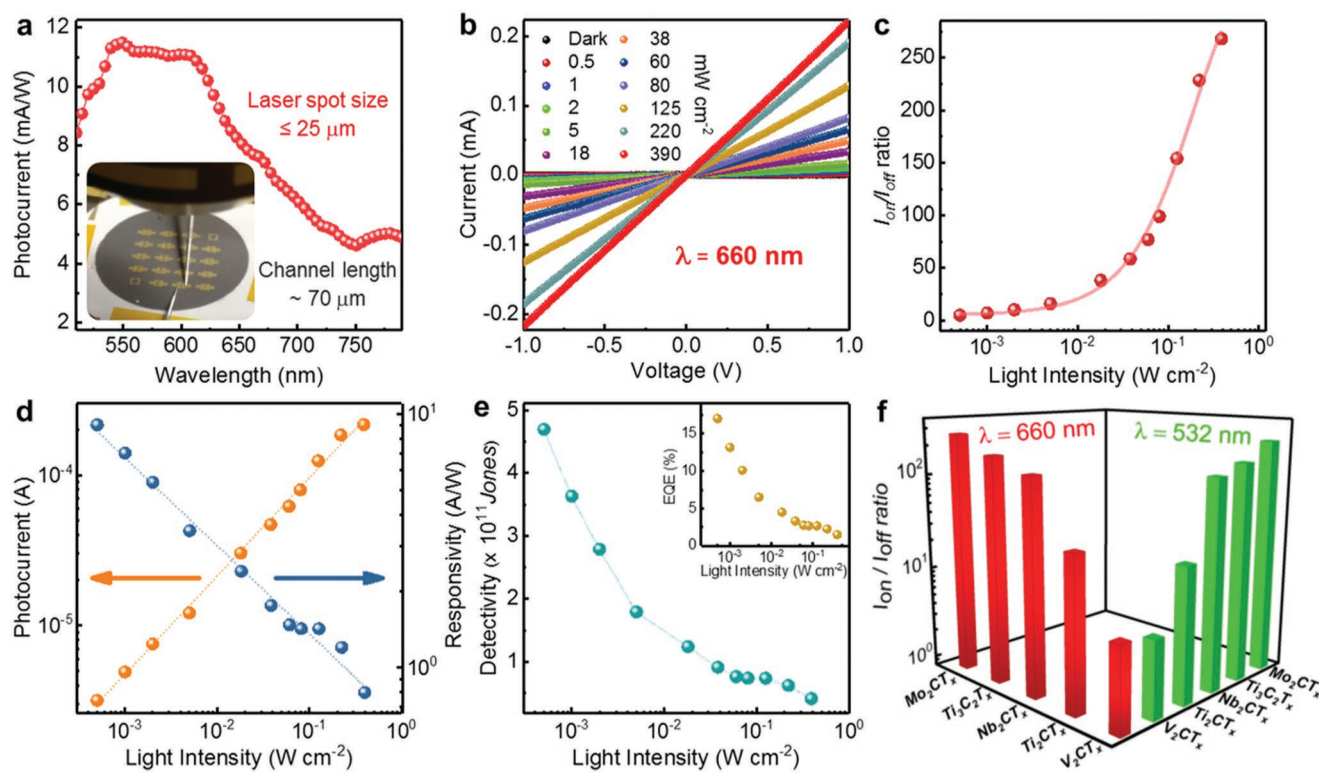

Figure 2. a) Photoresponse of a Mo$_2$CT$_x$ thin film photodetector as a function of wavelength, under 0.7 V bias voltage. Inset: Photograph of the photocurrent setup showing one of the investigated samples, illumination objective, and the contact electrodes. The spot size of the supercontinuum white laser excitation was ≤25 μm. b) Linear scale current–voltage (I–V) characteristics of the Mo$_2$CT$_x$ thin film photodetector in the dark and under different light intensities at a wavelength of 660 nm with a bias voltage of ±1 V. c) Ratios of the photocurrent to the dark current of the Mo$_2$CT$_x$ thin film photodetector as function of different light intensities. d) (Left) Photocurrents of the Mo$_2$CT$_x$ thin film photodetector as a function of different light intensities with respect to the dark state of the device. (Right) Responsivity of the photodetector as a function of different light intensities. e) The detectivity and EQE (inset) of the photodetector as a function of different light intensities. f) Ratios of the photocurrent of different MXene photodetectors with respect to the dark current, measured at wavelengths of 660 nm (red bars) and 532 nm (green bars). All the values were obtained at light intensities of 0.39 and 0.41 W cm^{-2} for wavelengths of 660 and 532 nm, respectively. Results shown in (c–e) are obtained considering an excitation at 660 nm.

**ADVANCED
SCIENCE NEWS**

www.advancedsciencenews.com

**ADVANCED
MATERIALS**

www.advmat.de

superimposed on a bias-dependent current ground level (refer to the Supporting Information for more details). On a side note, it has not escaped our notice to consider any possible photo-absorption by the oxidized Mo species (see Figure 1i). However, such Mo oxidized species (e.g., MoO_3 and/or Mo_4O_{11}) are known to have wide a band gap of ≈3.2 eV or even larger,[32,37–41] which rules out the possibility of their contribution in the visible photoresponse of our Mo_2CT_x thin films.

Following the spectral response depicted in Figure 2a, we examined the visible light detection of Mo_2CT_x thin films, under ambient conditions, at a representative wavelength of 660 nm with various light intensities. The linear and symmetrical behavior of the $I–V$ curves of the Mo_2CT_x (Figure 2b) indicates an Ohmic contact has formed between the thin film and Au electrodes. The current gradually increases with the light intensity, as a result of the incremented number of excited carriers, yielding a maximum I_{on}/I_{off} ratio of ≈2×10^2 at a light intensity and bias voltage of 0.39 W cm^{-2} and 1 V, respectively, as shown in Figure 2c. The I_{on}/I_{off} ratio for the Mo_2CT_x thin film as a function of film thickness demonstrates a saturation effect indicating a photocurrent level almost independent of the film thickness in the range from 1.5 to 4.0 µm (Figure S17, Supporting Information), that characterizes the full coverage of the substrate. The photocurrent is obtained at different incident light intensities by subtracting the dark current from the current recorded under illumination (Figure 2d). The photocurrent strongly depends on the incident light intensities and increases steeply from 1×10^{-6} to 2×10^{-4} A as the light intensity increases from 5×10^{-4} to 0.39 W cm^{-2}.

To evaluate the performance of the Mo_2CT_x photodetectors, their responsivity (R), specific detectivity (D^*), and external quantum efficiency (EQE) were calculated under incident light of 660 nm and a bias voltage of −1 V and are presented in Figure 2d,e. R, D^*, and EQE are calculated based on previous reports with the assumption that the dark current is primarily dominated by the shot noise (Table S2, Supporting Information).[42–44] At light intensities as low as 5×10^{-4} W cm^{-2}, our device reaches a responsivity of 9 A W^{-1} and decreases with increasing light intensity (Figure 2d). The drop in responsivity is attributed to the filling of the trap states present in the Mo_2CT_x thin film that might be originated from the defects and/or surface-terminated functional groups. Besides, increasing the illumination at high level enhances the recombination of generated hot carriers while progressively reduces the density of available states in the conduction band, resulting in a saturation of the photocurrent and a gradual decrease in the R.[45] The calculated maximum D^* and EQE, under illumination of 660 nm, are 4.7×10^{11} Jones and 17, respectively, and they gradually decrease with increasing light intensity (Figure 2d). In addition, our solution-processed Mo_2CT_x photodetector arrays demonstrate very high cell-to-cell and batch-to-batch reliabilities (Figure S18, Supporting Information).

We also examined the photodetection performance of Mo_2CT_x at another visible wavelength of 532 nm (Figure S19, Supporting Information), and it exhibited similar performance to that obtained at 660 nm, which correlates with the broad visible band selectivity shown in Figure 2a. The visible-light photoresponse of other MXene compositions was also studied and the results are summarized in Figure 2f, and Figures S20

and S21 in the Supporting Information. All of the photodetectors responded to the 660 and 532 nm light with little variation in the detection performance, which depends on the characteristic optical absorption, electrical conductivity, and free carrier concentration of the individual MXenes.

In view of the broadband absorption of Mo_2CT_x (Figure 1d), we also examined our devices under UV (325 nm) and NIR (1064 nm) illumination, near both edges of the visible band. Interestingly, despite being within the free carrier absorption regime as indicated by the UV–vis–NIR absorption spectra in Figure 1d, very weak photoresponse was obtained at both spectral ranges (Figure S22, Supporting Information). We attribute this to the presence of characteristic surface plasmons (SPs), collective oscillations of free carriers, supported by Mo_2CT_x nanosheets. In principle, the possibility to excite an SP resonating at the same frequency of incident light is known to enhance the device performance of many applications and is the distinctive characteristic of a plasmonic device. Hence, we believe that our devices have lower performances at nonvisible wavelengths because they do not match any of the resonance frequencies of the SPs that are potentially supported by the Mo_2CT_x nanosheets. A thorough explanation for our hypothesis is provided in the Supporting Information, where we discuss the physical electromechanical properties of a multilayer Mo_2CT_x cluster in comparison with gold as a typical example for conventional plasmonic materials.

To validate our hypothesis, we implemented a combination of STEM and ultrahigh resolution EELS to investigate the presence of SPs supported by multilayer Mo_2CT_x nanosheets. **Figure 3**a displays a typical low-loss EEL spectra (with zero-loss-peak (ZLP) subtracted) of Mo_2CT_x with four distinct features, identified at 0.3, 0.39, 2.45, and 3.42 eV. The obtained EELS intensity distribution maps at each feature are shown in the inset of Figure 3a along with the annular dark field (ADF) STEM micrograph of a truncated triangular Mo_2CT_x nanosheet (58 nm thick). We interpret the peaks at 0.3 and 0.39 eV as the dipole and quadrupole longitudinal modes, respectively, of the SP supported by the Mo_2CT_x nanosheet. Analogous distinct multipolar modes have also been reported for $Ti_3C_2T_x$ nanosheets.[19] The peak at 2.45 eV, distinguished with its homogeneous distribution, is assigned to the transversal SP mode, which is size-independent and solely related to the free electron concentration. Further discussion about the differences between longitudinal and transversal SP modes is provided in the STEM/EELS characterization section in the Supporting Information. The EELS absorption edge with an onset at 3.42 eV is ascribed to the interconduction band transitions as well as the IBT extending up to 7 eV. EELS maps of SPs for other Mo_2CT_x and $Ti_3C_2T_x$ nanosheets are depicted in Figures S23–S28 in the Supporting Information.

In principle, our EELS results suggest that the Mo_2CT_x devices would only work at wavelengths in resonance with the supported SPs, be it longitudinal or transversal modes. However, owing to the low resonance energy levels (mid-IR range) of the longitudinal modes, which are beyond the capability of our photoexcitation sources, we directed our attention to the transversal SP mode (refer to the Supporting Information for more details about the nature of the longitudinal and transversal SP modes). The energy window of the transversal
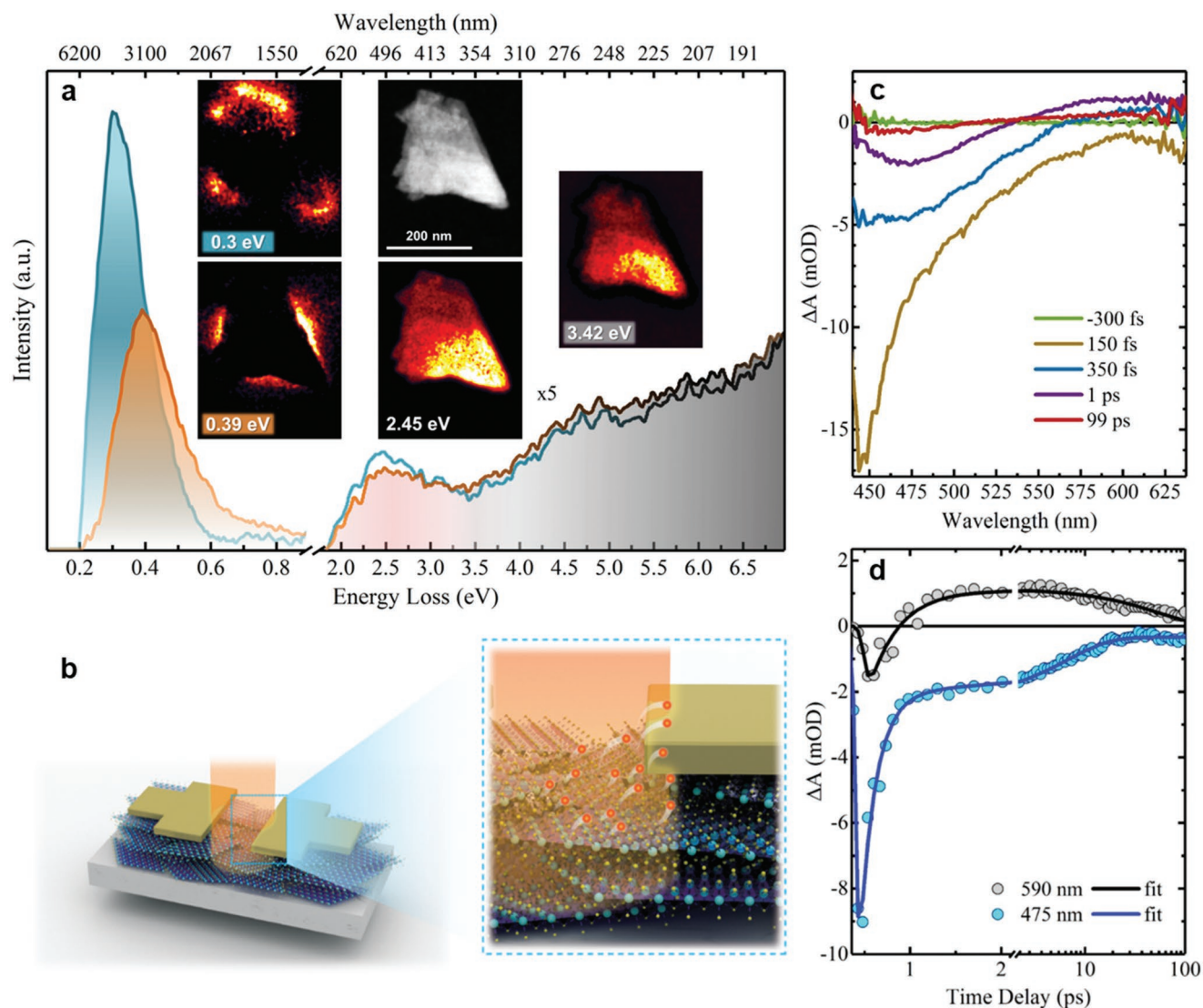
Figure 3. a) ZLP-subtracted EELS acquired on a truncated triangular nanosheet of Mo_2CT_x ($\approx$58 nm ± 1 at the center). The spectra are normalized to the transversal SP peak at 2.45 eV (highlighted in red) and magnified by a factor of 5 above 1.7 eV. Insets: ADF-STEM micrograph of the Mo_2CT_x nanosheet on a Si_3N_4 supporting membrane (black area), and the EELS fitted intensity maps of the corresponding longitudinal SP modes; namely, dipole (0.3 eV) and quadrupole (0.39 eV), in addition to the transversal SP mode (2.45 eV) and the IBT (starting at 3.42 eV). b) Schematic representation of the photodetector under illumination showing the migration process of the plasmon-assisted hot electrons toward the biased gold electrodes. c) Time-resolved visible transient absorption spectra of Mo_2CT_x at different time slots. d) Kinetic traces of the GSB recovery and ESA decay of Mo_2CT_x extracted at 475 and 590 nm, respectively. These data were collected under excitation wavelength of 330 nm.

SP mode is highlighted in red in Figure 3a, and in the ellipsometric results obtained for Mo_2CT_x thin films (see Figure S29 and Table S3, Supporting Information). Once the photoactive Mo_2CT_x thin film is illuminated at wavelengths with matching resonance, plasmon-assisted hot carriers are generated and efficiently separated to the Au electrodes maintained under an applied electric field. We believe that the photocurrent generation in Mo_2CT_x is principally controlled by plasmon-assisted hot electrons, with marginal photo-thermoelectric and bolometric effects (Figure S30, Supporting Information).[7,27] The schematic representation in Figure 3b illustrates the migration process of the plasmon-assisted hot carriers toward the biased gold electrodes. These results not only correlate very well with

our hypothesis but are also considered as the first report evidencing SPs in MXenes other than $Ti_3C_2T_x$.

To elucidate the dynamics of the generated plasmon-assisted hot carriers, i.e., electrons, upon excitation, we conducted femtosecond visible transient absorption measurements for our MXene nanosheets. Figure 3c shows the transient spectra of Mo_2CT_x nanosheets obtained under UV-laser excitation of 330 nm. The transient absorption spectra are characterized by a strong ground state bleach (GSB), maximized at $\approx$450 nm at early times. Generally, in 2D sheets, the plasmon peaks are expected to be broad and featureless due to high damping effect form electron–phonon interactions.[46,47] In our measurement, the GSB underwent an ultrafast process

within ≈200 fs, in which the GSB diminished, and simultaneously a positive feature, excited state absorption (ESA), centralized at ≈590 nm, evolved. Such an ultrafast femtosecond process corroborates the existence of SPs as evidenced by EELS. Subsequently, both GSB and ESA recovered into zero with time scales of ≈13 and 53 ps, respectively. The lifetimes were extracted by fitting the kinetic traces at 475 and 590 nm as shown in Figure 3d. The observed dynamics are attributed to the following processes: 1) After photon excitation, SPs were directly populated within 120 fs (temporal resolution of our technique), as reflected by the strong GSB at early times.[48] 2) According to Landau damping model, the plasmon can transfer its energy to the formation of an electron–hole pair, with a time scale of ≈100 fs, for metallic materials.[48–50] However, in our case, this process took about 200 fs to occur, in which the formation of ESA is attributed to the electron features, while the strong quenching of GSB is ascribed to the hole features. 3) Following the electron–hole formation, the recombination process for the electron was ≈53 ps, and ≈13 ps for the hole. This variation in lifetimes can be attributed to the presence of active hole-trapping sites that are filled afterward by the populated electrons within 53 ps. The relatively slow recombination dynamics compared to classical plasmonic metals can be attributed to the absence of metallic structures as previously reported.[46] Such slow relaxation is indicative of scattering with phonons and few other electrons, which correlates well with unexpected S/AS intensity ratios observed in the low-frequency Raman. This finding concurs with the relatively low free carrier density ≈10^{20} cm^{-3},[7] which is ≈4 orders lower than metals. To the best of our knowledge, this is the first report for ultrafast visible transient absorption of any MXene. We also obtained the kinetic traces of $Ti_3C_2T_x$ along with their extracted lifetimes (Figure S31, Supporting Information).

Next, we investigated the dynamic performance of Mo_2CT_x photodetector by measuring their response time for the rise and decay of the photocurrent upon switching the light ON and OFF. **Figure 4**a shows the photocurrent of the photodetector under alternating ON and OFF cycles at a wavelength of 660 nm with a light intensity of 0.22 W cm^{-2}. The photocurrent of the Mo_2CT_x thin films sharply rose and decayed upon multiple switching cycles at the millisecond level, demonstrating good reliability and reversibility of the photodetector. To check the stability of the photodetectors, the photocurrent was measured under continuous illumination of 660 nm light in ambient conditions, as shown in Figure 4b. The device maintained over 80% of the initial photocurrent even after 12 000 s. In addition, our air-exposed Mo_2CT_x thin film channel exhibits weak charge transfer between Mo_2CT_x and the absorbed O_2 or H_2O molecules, such that only less excited carriers (hot electrons) contribute to the charge transfer, and thus a stable photodetection operation was achieved.[51,52] In order to verify the charge-transfer effect, we measured the dark current of the Mo_2CT_x in air and in vacuum. The dark current measured in air for Mo_2CT_x films was not different from that measured under vacuum (Figure S32, Supporting Information), suggesting that the devices have no significant interaction with the ambient H_2O or O_2 molecules. Besides, the high photostability of our Mo_2CT_x nanosheets can be ascribed to their high

crystal quality and few nanometer-scale defects (Figure 1b,c), which benefits the structural and chemical integrity of the device. On the other hand, the stability of the $Ti_3C_2T_x$ MXene thin film is strongly deteriorated with increasing illumination time (Figure S33, Supporting Information). The spontaneous partial oxidation of $Ti_3C_2T_x$ MXene[14] leads to the formation of titanium oxides (e.g., TiO_2), on which O_2 molecules are generally known to be adsorbed.[53] In consequence, the air-exposed $Ti_3C_2T_x$-TiO_2 hybrid channel exhibits strong charge-transfer effect between TiO_2 and the adsorbed O_2, allowing for the contribution of more photoinduced carriers in the charge transfer process, and thus decreasing the stability. This analogy was further confirmed by obtaining the dark current of $Ti_3C_2T_x$ films in vacuum and in air. The dark current measured in vacuum was significantly higher than that measured in air, confirming the strong charge-transfer effect between TiO_2 and O_2 molecules.

Meanwhile, the stability of the fabricated photodetectors was checked as a function of storage time, where no obvious deterioration has been observed. The I_{on}/I_{off} ratio remained almost the same over the course of more than 30 days of storage inside a vacuum desiccator (Figure 4c). These results suggest that the Mo_2CT_x thin film devices are stable under vacuum storage conditions, highlighting their stable and durable photodetection operation. However, their stability in oxygen-containing environments remains to be properly investigated. Moreover, knowing that MXenes have demonstrated excellent mechanical flexibility,[54] we investigated the photodetection properties of Mo_2CT_x thin films under various mechanical deformations (different bending radii). The initial I_{on}/I_{off} ratio values, obtained at 660 nm, as a function of the bending radius, remained unaltered even at a bending radius of ≈3 mm (see Figure 4d). A similar performance was also obtained after 500 bending cycles in the outward direction with a bending radius of ≈3 mm, without any significant deterioration in the performance (Figure 4e). The arrays of Mo_2CT_x thin film photodetectors, fabricated on nylon membranes, are readily bendable under multiple and repeated deformations. This illustrates their potential for harsh optoelectronics against mechanical stress and other flexible applications.

In summary, we have fabricated flexible MXene thin film photodetectors operating in the visible spectral region. Their photoresponse is dominated by the intrinsic plasmon-assisted hot carrier generation without the need for integration with other metallic plasmonic structures, as previously demonstrated with several 2D materials.[55] Despite being the first demonstration of plasmonic photodetection in MXenes, the performance of Mo_2CT_x thin films considering their R and D^* is surpassing the majority of previously reported visible-band photodetectors based on solution-processed 2D materials. A comparison of several literature reports is summarized in Table S4 in the Supporting Information. In addition to their attractive performance and solution processability, we have revealed that our MXene-based devices possess additional set of advantages including full visible spectrum coverage, highly stable operation, and mechanical flexibility. On the top of that, by means of high-resolution STEM-EELS, we have been able, for the first time, to image the spatial and energy distribution of SP modes over individual Mo_2CT_x nanosheets. Further, using
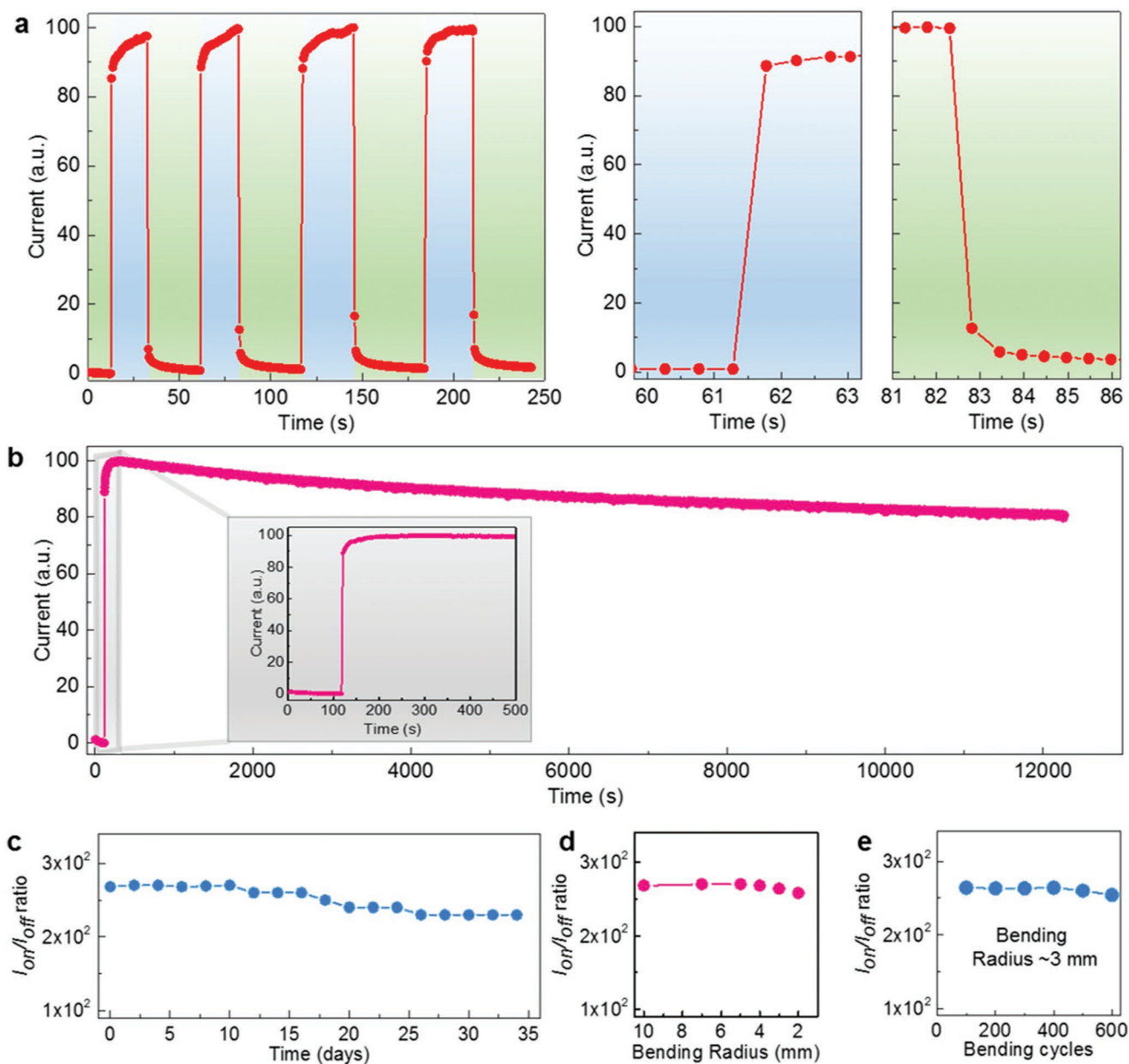
Figure 4. a) Photoresponse behavior of Mo_2CT_x thin film photodetector under alternating ON and OFF cycles at a wavelength of 660 nm with a light intensity of 0.22 W cm^{-2}. Both the switch-ON and -OFF times of the detector were ≈500 ms. b) Photostability of the Mo_2CT_x thin film photodetectors under continuous illumination of 660 nm light in ambient conditions. The device maintained ≈80% of the initial photocurrent even after ≈12 000 s. c) Ratios of the photocurrent, under 660 nm light illumination, with respect to the dark current as a function of storage time. d) Photocurrent and dark current ratio as a function of the bending radius. e) Ratios of the photocurrent to the dark current of the photodetectors as a function of the number of bending cycles at a bending radius of ≈3 mm. Devices worked properly after 500 bending cycles at a bending radius of ≈3 mm, without any significant deterioration of the performance. All of the values were obtained at a wavelength of 660 nm with a light intensity of 0.22 W cm^{-2}.

femtosecond visible transient absorption measurements, we probed the ultrafast dynamics of the photoactive carriers supported by Mo_2CT_x nanosheets. The demonstrated ability of coupling with light and dephasing of SPs with a short lifetime have led to a photoresponse outperforming that of photoelectron-based semiconductor devices. Our findings shed light on the knowledge of photocurrent generation mechanisms in MXenes, making them much more viable for many photonic and plasmonic device applications.

Experimental Section

Experimental details including various MAX and MXene syntheses, device fabrication, and several characterizations can be found in the Supporting Information.

Supporting Information

Supporting Information is available from the Wiley Online Library or from the author.

Conflict of Interest

The authors declare no conflict of interest.

[1] M. Naguib, M. Kurtoglu, V. Presser, J. Lu, J. Niu, M. Heon, L. Hultman, Y. Gogotsi, M. W. Barsoum, *Adv. Mater.* **2011**, *23*, 4248.

[2] B. Anasori, M. R. Lukatskaya, Y. Gogotsi, *Nat. Rev. Mater.* **2017**, *2*, 16098.

[3] M. Ghidiu, M. R. Lukatskaya, M.-Q. Zhao, Y. Gogotsi, M. W. Barsoum, *Nature* **2014**, *516*, 78.

[4] F. Shahzad, M. Alhabeb, C. B. Hatter, B. Anasori, S. Man Hong, C. M. Koo, Y. Gogotsi, *Science* **2016**, *353*, 1137.

[5] Y.-Z. Zhang, K. H. Lee, D. H. Anjum, R. Sougrat, Q. Jiang, H. Kim, H. N. Alshareef, *Sci. Adv.* **2018**, *4*, eaat0098.

[6] P. Nayak, Q. Jiang, R. Mohanraman, D. Anjum, M. N. Hedhili, H. N. Alshareef, *Nanoscale* **2018**, *10*, 17030.

[7] H. Kim, B. Anasori, Y. Gogotsi, H. N. Alshareef, *Chem. Mater.* **2017**, *29*, 6472.

[8] L. Ding, Y. Wei, L. Li, T. Zhang, H. Wang, J. Xue, L.-X. Ding, S. Wang, J. Caro, Y. Gogotsi, *Nat. Commun.* **2018**, *9*, 155.

[9] K. Maleski, V. N. Mochalin, Y. Gogotsi, *Chem. Mater.* **2017**, *29*, 1632.

[10] O. Mashtalir, M. Naguib, V. N. Mochalin, Y. Dall'Agnese, M. Heon, M. W. Barsoum, Y. Gogotsi, *Nat. Commun.* **2013**, *4*, 1716.

[11] M. Naguib, V. N. Mochalin, M. W. Barsoum, Y. Gogotsi, *Adv. Mater.* **2014**, *26*, 992.

[12] Y. Dong, S. S. K. Mallineni, K. Maleski, H. Behlow, V. N. Mochalin, A. M. Rao, Y. Gogotsi, R. Podila, *Nano Energy* **2018**, *44*, 103.

[13] Q. Jiang, C. Wu, Z. Wang, A. C. Wang, J.-H. He, Z. L. Wang, H. N. Alshareef, *Nano Energy* **2018**, *45*, 266.

[14] S. Chertopalov, V. N. Mochalin, *ACS Nano* **2018**, *12*, 6109.

[15] Z. Wang, H. Kim, H. N. Alshareef, *Adv. Mater.* **2018**, *30*, 1706656.

[16] Y. Dong, S. Chertopalov, K. Maleski, B. Anasori, L. Hu, S. Bhattacharya, A. M. Rao, Y. Gogotsi, V. N. Mochalin, R. Podila, *Adv. Mater.* **2018**, *30*, 1705714.

[17] A. D. Dillon, M. J. Ghidiu, A. L. Krick, J. Griggs, S. J. May, Y. Gogotsi, M. W. Barsoum, A. T. Fafarman, *Adv. Funct. Mater.* **2016**, *26*, 4162.

[18] G. Li, K. Kushnir, Y. Dong, S. Chertopalov, A. M. Rao, V. N. Mochalin, R. Podila, L. V. Titova, *2D Mater.* **2018**, *5*, 035043.

[19] J. K. El-Demellawi, S. Lopatin, J. Yin, O. F. Mohammed, H. N. Alshareef, *ACS Nano* **2018**, *12*, 8485.

[20] V. Mauchamp, M. Bugnet, E. P. Bellido, G. A. Botton, P. Moreau, D. Magne, M. Naguib, T. Cabioc'h, M. W. Barsoum, *Phys. Rev. B* **2014**, *89*, 235428.

[21] K. Chaudhuri, M. Alhabeb, Z. Wang, V. M. Shalaev, Y. Gogotsi, A. Boltasseva, *ACS Photonics* **2018**, *5*, 1115.

[22] X. Jiang, S. Liu, W. Liang, S. Luo, Z. He, Y. Ge, H. Wang, R. Cao, F. Zhang, Q. Wen, J. Li, Q. Bao, D. Fan, H. Zhang, *Laser Photonics Rev.* **2018**, *12*, 1700229.

[23] F. Xia, T. Mueller, Y.-M. Lin, A. Valdes-Garcia, P. Avouris, *Nat. Nanotechnol.* **2009**, *4*, 839.

[24] Z. Yin, H. Li, H. Li, L. Jiang, Y. Shi, Y. Sun, G. Lu, Q. Zhang, X. Chen, H. Zhang, *ACS Nano* **2012**, *6*, 74.

[25] G. V. Hartland, L. V. Besteiro, P. Johns, A. O. Govorov, *ACS Energy Lett.* **2017**, *2*, 1641.

[26] S. Adachi, *Optical Properties of Crystalline and Amorphous Semiconductors*, Springer, Boston, MA, **1999**.

[27] J. Halim, S. Kota, M. R. Lukatskaya, M. Naguib, M.-Q. Zhao, E. J. Moon, J. Pitock, J. Nanda, S. J. May, Y. Gogotsi, M. W. Barsoum, *Adv. Funct. Mater.* **2016**, *26*, 3118.

[28] Z. W. Seh, K. D. Fredrickson, B. Anasori, J. Kibsgaard, A. L. Strickler, M. R. Lukatskaya, Y. Gogotsi, T. F. Jaramillo, A. Vojvodic, *ACS Energy Lett.* **2016**, *1*, 589.

[29] C. C. Lai, R. Meshkian, M. Dahlqvist, J. Lu, L. Å. Näslund, O. Rivin, E. N. Caspi, O. Ozeri, L. Hultman, P. Eklund, M. W. Barsoum, J. Rosen, *Acta Mater.* **2015**, *99*, 157.

[30] J. Halim, K. M. Cook, M. Naguib, P. Eklund, Y. Gogotsi, J. Rosen, M. W. Barsoum, *Appl. Surf. Sci.* **2016**, *362*, 406.

[31] J. Baltrusaitis, B. Mendoza-Sanchez, V. Fernandez, R. Veenstra, N. Dukstiene, A. Roberts, N. Fairley, *Appl. Surf. Sci.* **2015**, *326*, 151.

[32] K. Inzani, M. Nematollahi, F. Vullum-Bruer, T. Grande, T. W. Reenaas, S. M. Selbach, *Phys. Chem. Chem. Phys.* **2017**, *19*, 9232.

[33] A. Borgschulte, O. Sambalova, R. Delmelle, S. Jenatsch, R. Hany, F. Nüesch, *Sci. Rep.* **2017**, *7*, 40761.

[34] C. R. Clayton, Y. C. Lu, *Surf. Interface Anal.* **1989**, *14*, 66.

[35] J. Światowska-Mrowiecka, S. de Diesbach, V. Maurice, S. Zanna, L. Klein, E. Briand, I. Vickridge, P. Marcus, *J. Phys. Chem. C* **2008**, *112*, 11050.

[36] M. Rouhani, Y. L. Foo, J. Hobley, J. Pan, G. S. Subramanian, X. Yu, A. Rusydi, S. Gorelik, *Appl. Surf. Sci.* **2013**, *273*, 150.

[37] S. Bandaru, G. Saranya, N. J. English, C. Yam, M. Chen, *Sci. Rep.* **2018**, *8*, 10144.

[38] S. Balendhran, J. Deng, J. Z. Ou, S. Walia, J. Scott, J. Tang, K. L. Wang, M. R. Field, S. Russo, S. Zhuiykov, M. S. Strano, N. Medhekar, S. Sriram, M. Bhaskaran, K. Kalantar-Zadeh, *Adv. Mater.* **2013**, *25*, 109.

[39] G. E. Buono-Core, A. H. Klahn, C. Castillo, E. Muñoz, C. Manzur, G. Cabello, B. Chornik, *J. Non-Cryst. Solids* **2014**, *387*, 21.

[40] D. V. Pham, R. A. Patil, J.-H. Lin, C.-C. Lai, Y. Liou, Y.-R. Ma, *Nanoscale* **2016**, *8*, 5559.

[41] A. Bouzidi, N. Benramdane, H. Tabet-Derraz, C. Mathieu, B. Khelifa, R. Desfeux, *Mater. Sci. Eng., B* **2003**, *97*, 5.

[42] X. Gong, M. Tong, Y. Xia, W. Cai, J. S. Moon, Y. Cao, G. Yu, C.-L. Shieh, B. Nilsson, A. J. Heeger, *Science* **2009**, *325*, 1665.

[43] D. B. Velusamy, M. A. Haque, M. R. Parida, F. Zhang, T. Wu, O. F. Mohammed, H. N. Alshareef, *Adv. Funct. Mater.* **2017**, *27*, 1605554.

[44] N. Huo, G. Konstantatos, *Adv. Mater.* **2018**, *30*, 1801164.

[45] O. Lopez-Sanchez, D. Lembke, M. Kayci, A. Radenovic, A. Kis, *Nat. Nanotechnol.* **2013**, *8*, 497.

[46] A. S. Rubio, *Modified Au-Based Nanomaterials Studied by Surface Plasmon Resonance Spectroscopy*, Springer, Cham, **2015**.

[47] P. Narang, R. Sundararaman, A. Atwater Harry, *Nanophotonics* **2016**, *5*, 96.

[48] M. L. Brongersma, N. J. Halas, P. Nordlander, *Nat. Nanotechnol.* **2015**, *10*, 25.

[49] W. Li, G. Valentine Jason, *Nanophotonics* **2017**, *6*, 177.

**ADVANCED
SCIENCE NEWS**

www.advancedsciencenews.com

**ADVANCED
MATERIALS**

www.advmat.de

[50] E. Cortés, W. Xie, J. Cambiasso, A. S. Jermyn, R. Sundararaman, P. Narang, S. Schlücker, S. A. Maier, *Nat. Commun.* **2017**, *8*, 14880.

[51] D. B. Velusamy, R. H. Kim, S. Cha, J. Huh, R. Khazaeinezhad, S. H. Kassani, G. Song, S. M. Cho, S. H. Cho, I. Hwang, J. Lee, K. Oh, H. Choi, C. Park, *Nat. Commun.* **2015**, *6*, 8063.

[52] M. M. Furchi, D. K. Polyushkin, A. Pospischil, T. Mueller, *Nano Lett.* **2014**, *14*, 6165.

[53] J. Zou, Q. Zhang, K. Huang, N. Marzari, *J. Phys. Chem. C* **2010**, *114*, 10725.

[54] Z. Ling, C. E. Ren, M.-Q. Zhao, J. Yang, J. M. Giammarco, J. Qiu, M. W. Barsoum, Y. Gogotsi, *Proc. Natl. Acad. Sci. USA* **2014**, *111*, 16676.

[55] F. H. L. Koppens, T. Mueller, P. Avouris, A. C. Ferrari, M. S. Vitiello, M. Polini, *Nat. Nanotechnol.* **2014**, *9*, 780.

1807658 (10 of 10)